



Photocatalytic hydrogen evolution and bacterial inactivation utilizing sonochemical-synthesized g-C₃N₄/red phosphorus hybrid nanosheets as a wide-spectral-responsive photocatalyst: The role of type I band alignment



Wanjun Wang^a, Guiying Li^a, Taicheng An^{a,*}, Donald K.L. Chan^b, Jimmy C. Yu^{b,*}, Po Keung Wong^c

^a Guangzhou Key Laboratory of Environmental Catalysis and Pollution Control, School of Environmental Science and Engineering, Institute of Environmental Health and Pollution Control, Guangdong University of Technology, Guangzhou, 510006, China

^b Department of Chemistry and Institute of Environment, Energy and Sustainability, The Chinese University of Hong Kong, Shatin, N.T., Hong Kong, China

^c School of Life Sciences, The Chinese University of Hong Kong, Shatin, N.T., Hong Kong, China

ARTICLE INFO

Keywords:

Photocatalytic activity
Sonochemical synthesis
g-C₃N₄
Red phosphorus
Type I heterojunction

ABSTRACT

Efficient sunlight harvesting is imperative in the design of ideal photocatalysts for both environmental and energy applications. In this study, a wide-spectral-responsive photocatalyst composed of g-C₃N₄/red P (CNP) hybrid nanosheets was developed by a one-step “green” sonochemical method at room temperature. Ultrasound irradiation causes exfoliation of the layered g-C₃N₄, downsizing the red P particles and anchoring them onto the g-C₃N₄ nanosheets to form intimate CNP heterojunctions. As a dual active center photocatalyst, the CNP heterostructures exhibit significantly enhanced photocatalytic activity both for H₂ evolution and bacterial inactivation under visible light irradiation. In addition, the responsive wavelength of this new-fabricated photocatalyst can be extended to 700 nm. The crucial role of type I band alignment between g-C₃N₄ and red P is illuminated to facilitate the interface charge separation and extend the light response by efficiently utilizing the photogenerated e⁻ excited from both g-C₃N₄ and red P. Moreover, a direct h⁺ oxidation mechanism rather than a e⁻ reduction mechanism is also found for bacterial inactivation under anaerobic conditions. This work provides a general strategy to fabricate novel metal-free heterostructures with wide-spectral-responsive photocatalytic activity by taking advantage of the type I band alignment combined with the narrow band gap feature of elemental red P.

1. Introduction

Solar-driven hydrogen (H₂) production via photocatalytic water splitting is a promising strategy for solving the future energy crisis [1–3]. Meanwhile, water disinfection by photocatalysis has recently attracted increasing attention due to its potential of solar energy conversion for bacterial inactivation [4–7]. Therefore, photocatalytic technology holds great promise for solving both energy and environmental problems which are two of the major problems facing the human society. Thus, it is very attractive to develop cost-effective photocatalysts that have both H₂ evolution and bacterial inactivation activity. On the other hand, in order to utilize the whole solar energy, it is crucial to develop active photocatalytic systems working under longer visible wavelengths (e.g. 400–700 nm). However, the decrease of band gap of a semiconductor to extend the light response would inevitably cause the deterioration of photo-generated e⁻-h⁺ redox ability and fast recombination of charge carriers. To solve this problem,

heterojunction has been generally adopted to promote the dissociation of excitons and facilitate the subsequent collection and separation of charge at the interfaces of two semiconductors, minimizing charge recombination during past decades. In general, two kinds of heterojunction is often used in photocatalysis, namely type I (i.e. straddling gap) and type II (i.e. staggered gap) band alignment. The type II heterojunction has been extensively reported recently, such as the well-known TiO₂/CdS [8], SrTO₃/TiO₂ [9], Fe₂O₃/TiO₂ [10], etc. In contrast, type I heterojunction has seldom been regarded as the first choice in the field of photocatalyst design, because both the photo-generated e⁻ and h⁺ of semiconductor are transferred to the other semiconductor at the interfaces, which results in the decrease of redox ability of the charge carriers. However, the type I heterojunction has unique advantages of being able to extract both e⁻ and h⁺ from one semiconductor to the other semiconductor. If the other semiconductor has a relatively wide light absorption, a wide-spectral-responsive composite photocatalyst with efficient charge separation may be achieved by applying the type I

* Corresponding authors.

E-mail addresses: antc99@gdut.edu.cn, antc99@163.com (T. An), jimyu@cuhk.edu.hk (J.C. Yu).

alignment. However, the role of type I heterojunction in photocatalyst design has not been fully illuminated in previous studies.

One of the primary mission for the real application of photocatalysis is to develop cost-effective photocatalyst that can be synthesized by environmental benign methods without the use of toxic compounds at room temperature. Recently, graphitic carbon nitride ($\text{g-C}_3\text{N}_4$) has attracted worldwide attention [11–15]. Although it shows high photocatalytic activity under VL irradiation shorter than 460 nm, it exhibits very low activity at longer wavelength irradiation due to its relatively large band gap of 2.7 eV [11]. Very recently, red phosphorus (red P) was discovered by our group as a novel single-element photocatalyst for H_2 evolution [16,17], dye degradation [18] as well as bacterial inactivation [19]. It has become a promising photocatalyst for solar chemical energy conversion owing to its response to long wavelength photons up to 700 nm and its photo-stability up to 90 h under VL irradiation [16]. Thus, the coupling of $\text{g-C}_3\text{N}_4$ with red P may create a new wide-spectral-responsive photocatalytic system to fully utilize the whole solar energy, and it is interesting to fabricate $\text{g-C}_3\text{N}_4$ nanosheets anchored with elemental red P by a facile and "green" method for wide-spectral-responsive photocatalyst.

The red P/ $\text{g-C}_3\text{N}_4$ composites with large particles of red P and $\text{g-C}_3\text{N}_4$ have been synthesized by solid state annealing method [20] and by a chemical-vapor-deposition (CVD) method [21] previously, but the photocatalytic activity of both composite photocatalysts is by far from satisfactory. On the other hand, it has been reported that if bulk $\text{g-C}_3\text{N}_4$ is exfoliated into nanosheets, the photocatalytic activity will be significantly increased due to enhanced surface area providing more active sites [22,23], and sonochemistry has been proven to be an important synthetic tool for the exfoliation of layered materials into nanosheets, especially for the exfoliation of $\text{g-C}_3\text{N}_4$ [24,25]. The acoustic cavitation causes extreme effects locally, and the implosion of the cavitation bubble also results in the velocity of liquid jets up to 280 m/s [26] and strong hydrodynamic shear-forces up to 108 Pa [27]. Such extreme conditions in the liquid are expected to not only exfoliate $\text{g-C}_3\text{N}_4$, but also break large red P particles into nanosize. In addition, the ultrasound waves supply the high energy needed for chemical bonding between $\text{g-C}_3\text{N}_4$ and red P, resulting in the intimate contact at the interfaces for efficient charge transportation.

Herein, a $\text{g-C}_3\text{N}_4$ /red P hybrid nanosheet photocatalyst was synthesized by a simple sonochemical one-pot fabrication method at room temperature. The as-prepared $\text{g-C}_3\text{N}_4$ /red P nanosheets showed significantly enhanced photocatalytic activity than that of both $\text{g-C}_3\text{N}_4$ and red P for H_2 evolution under wide spectrum of VL irradiation (400–700 nm). And the wavelength-dependent photocatalytic bacterial inactivation activity was also evaluated by the $\text{g-C}_3\text{N}_4$ /red P for the first time. The weight ratio of $\text{g-C}_3\text{N}_4$ and red P was optimized and the role of type I band alignment were also investigated in detail. Most importantly, the photocatalysts are environmental benign and the synthesis method are cost-effective, showing great potential to be used in large-scale practical applications. This work will open an avenue not only for the development of wide-spectral-responsive photocatalysts utilizing type I heterojunction, but also for the "green" synthesis of 2D hybrid nanosheets at room temperature.

2. Experimental

2.1. Sample preparation

Commercial red P (International Laboratory, USA, 99.9%) was purified by hydrothermal method before use [17]. Bulk $\text{g-C}_3\text{N}_4$ was synthesized following the previous report [28]. In a typical procedure, 10 g melamine (Sinopharm, 99%) was heated at 550 °C for 4 h in static air with a heating rate of 2.3 °C/min. After cooling naturally, the resultant yellow agglomerates were milled into powder in an agate mortar for further use.

The $\text{g-C}_3\text{N}_4$ /red P hybrid nanosheets were synthesized by ultrasonic-

assisted wet chemical method, as shown in Fig. S1. Typically, 0.1 g bulk $\text{g-C}_3\text{N}_4$ powder and a certain amount (g) of purified red P were added into 40 mL distilled water. After stirring for 10 min, the mixture was exposed to ultrasonic irradiation (Elma TI-H-10, 35 kHz) for 4 h. Then, the $\text{g-C}_3\text{N}_4$ /red P hybrid nanosheets were separated by centrifugation from the suspension, and the unreacted large aggregates of $\text{g-C}_3\text{N}_4$ and red P at the bottom of the reaction vessel were removed. After drying at 50 °C under vacuum, the $\text{g-C}_3\text{N}_4$ /red P composites were obtained and denoted as CNP-X (X represents the added amount of red P(g)).

2.2. Characterization

X-ray diffraction (XRD) patterns were recorded with a Rigaku Smart Lab X-ray diffractometer using Cu K α 1 irradiation ($\lambda = 1.5406 \text{ \AA}$). The accelerating voltage and applied current were 40 kV and 40 mA, respectively. UV-vis diffuse reflectance spectrum (UV-vis DRS) was obtained for the dry-pressed disk sample using a Varian Cary 500 UV-vis spectrophotometer equipped with a labsphere diffuse reflectance accessory, and BaSO_4 was used as a reflectance standard in the UV-vis DRS experiment. The morphology of the product was characterized by scanning electron microscopy (FESEM, FEI, Quanta 400 FEG) and transmission electron microscopy (TEM, FEI Tecnai G2 Spirit). The structure of composite photocatalyst was characterized by a Fourier transform infrared spectrometer (FT-IR, Nicolet 670) at a resolution of 4 cm^{-1} . The surface electronic states were analyzed by X-ray photoelectron spectroscopy (XPS, PerkinElmer PHI 5000), and all the binding energy values were calibrated by using C1 s = 284.6 eV as a reference.

Photoelectrochemical measurements of composite photocatalyst were carried out on an electrochemical workstation (CHI 660D, Shanghai Chen Hua Instrument Company, China) with a conventional three electrode cell, using a Pt plate and a saturated Ag/AgCl electrode as counter electrode and reference electrode, respectively. The working electrode was prepared on indium-tin oxide (ITO) glasses, which was cleaned by sonication in chloroform, acetone and ethanol for 30 min, respectively. The glass was then rinsed with water and kept in isopropanol for 24 h. Five-milligrams of samples and 10 μL of Nafion solution (5 wt%) were dispersed in a 1 mL water/isopropanol mixed solvent (3:1 v/v) by sonication to form a homogeneous catalyst colloid. Then, 100 μL of the catalyst colloid was deposited onto the ITO glass with areas of about 1 cm^2 . The working electrodes were immersed in a 0.1 M Na_2SO_4 aqueous solution without other additive for 30 s before the measurement. Electrochemical impedance spectroscopy (EIS) displayed as a Nyquist plot was obtained in the frequency range of 0.05 Hz–10⁵ Hz with an AC perturbation signal of 5 mV.

2.3. Photocatalytic H_2 evolution

The photocatalytic H_2 evolution experiments were carried out in a Pyrex reaction cell connected with a closed gas circulation and evacuation system. 40 mg of photocatalyst were dispersed into 50 mL of aqueous solution containing 10 vol% triethanolamine (TEOA) as a sacrificial agent. The suspension was purged with argon to remove dissolved air before irradiation. 1% Pt was loaded onto the samples by photoreduction of H_2PtCl_6 [29]. The solution was irradiated by a 300 W xenon lamp equipped with a 420 nm cut-off filter. The amount of H_2 generated from photocatalytic water splitting was measured by Techcomp GC7900 gas chromatography with TCD detector and a capillary column (molecular sieve 5 Å). High purity nitrogen gas was used as a carrier gas. The dependence of H_2 evolution rate on the absorption wavelength of prepared photocatalyst was measured by using an appropriate band pass filter (420, 500, 550, 600, 650 and 700 nm, respectively). The intensity of the monochromatic light was averaged at 5 representative points by a light meter (LI-COR, USA) and the active area of the reactor was approximately 38.5 cm^2 . The apparent quantum efficiency (AQE) was measured and calculated according to the following Eq. (1):

$$\text{AQE} [\%] = \frac{\text{number of reacted electrons}}{\text{number of incident photons}} \times 100$$

$$= \frac{\text{number of evolved H}_2\text{ molecules} \times 2}{\text{number of incident photons}} \times 100 \quad (1)$$

2.4. Photocatalytic bacterial inactivation

Escherichia coli K-12 was chosen as the model bacteria to evaluate the photocatalytic inactivation efficiency of the prepared photocatalysts according to the reported method [30]. Bacterial cells were firstly cultured in Nutrient Broth growth medium at 37 °C for 16 h with shaking, and then harvested by centrifugation at 4000 rpm for 15 min. The bacterial pellets were then washed with sterilized saline solution (0.9% NaCl) three times in a centrifuge tube and re-suspended in a sterilized saline solution to obtain suitable concentration of *E. coli*. Then, 50 mg of the as-prepared photocatalyst was added into 50 mL solution containing 10⁷ cfu/mL bacterial suspensions. The solution was irradiated by a 300 W Xenon lamp equipped with different light filter as in the above H₂ production experiments. Then, at different time intervals, aliquot samples were collected and uniformly spread onto Nutrient Agar plates after serial dilutions of the sterilized saline solution. The plates were incubated at 37 °C for 24 h to determine the viable cell counting. All the inactivation experiments were conducted in triplicate.

3. Results and discussion

3.1. Photocatalyst characterization

The phase structures of the obtained g-C₃N₄/red phosphorus (CNP) samples were evaluated by X-ray diffraction (XRD). As shown in Fig. 1, for the bulk sample, two characteristic peaks of g-C₃N₄ located at 13.6° and 27.4° is observed, which can be assigned to the (100) and (002) plane of the typical graphitic layer structures, according to the reference [31]. The two peaks corresponding to 0.681 and 0.326 nm interlayer spacing are reported to be derived from the in-plane repeated units and the stacking of the conjugated aromatic systems in layered structure, respectively [32]. Remarkably, the intensities of these two peaks are significantly decreased after sonochemical treatment with red P, indicating the successfully exfoliation of bulk g-C₃N₄ into 2D material, nanosheets. However, no peaks of phosphorus species were observed in CNP samples, due to the amorphous nature of elemental red P.

The morphologies of as-prepared CNP samples were observed by SEM and TEM technology. Fig. 2(a) shows a typical SEM image of bulk g-C₃N₄, exhibiting a stacked layered structure with large particle size.

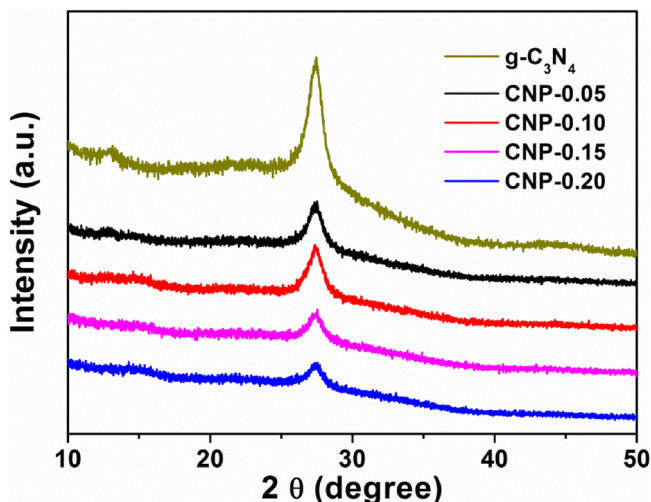


Fig. 1. X-Ray diffraction (XRD) patterns of the as-prepared CNP composites.

In contrast, the CNP-0.1 shows a sheet-like morphology anchored with lots of red P particles (Fig. 2(b)). TEM image in Fig. 2(c) further confirms the nanosheet morphology of the CNP hybrids. It is found that lots of small red P particles are anchored onto the g-C₃N₄ sheets, which is in-situ decorated onto the g-C₃N₄ sheets. In contrast, the pristine red P before sonochemical treatment shows large particles with sizes of several tens of micrometer (Fig. S2). This result indicates that the sonochemical method is not only able to exfoliate the layered g-C₃N₄, but also to break the large red P particles simultaneously at room temperature. The corresponding EDS spectrum in Fig. 2(d) clearly shows the elements of C, N, O and P, further confirming the successful loading of red P onto the exfoliated g-C₃N₄ nanosheets.

The functional groups of the samples were detected by FT-IR spectroscopy (Fig. S3). Several bands located in the 1200–1600 cm⁻¹ region are related to the typical stretching modes of aromatic C–N heterocycles in g-C₃N₄. The peak at about 810 cm⁻¹ represents tri-s-triazine unit mode. The broad band at 3000–3500 cm⁻¹ belongs to uncondensed terminal amino groups (–NH₂ or = NH groups) [33]. The FT-IR results well confirm the g-C₃N₄ structure in all the CNP samples, indicating the combination with red P does not affect the basic structure of g-C₃N₄. The vibrations of P-related group were hardly observed probably due to its overlapping with C–N bonds and the majority of phosphorus species exists in P⁰ states without chemical bonding with other elements. The pure red P shows several weak peaks at 500–600 cm⁻¹, which is attributed to the harmonics of bending O–P–O and O = P–O vibration in P₂O₅ according to reference [34], suggesting the existence of surface oxides in the red P. However, these peaks disappear in the CNP composites, indicating the surface oxides of red P was removed by sonochemical reactions.

To further confirm the chemical states of red P, XPS was also conducted and the results were shown in Fig. 3. The survey spectrum (Fig. 3(a)) shows that the CNP is mainly composed of C, N and P elements. For both g-C₃N₄ and CNP composites, the high-resolution N 1s spectra can be deconvoluted into two different peaks at binding energies of 398.8 and 400.7 eV (Fig. 3(b)), corresponding to the sp²-hybridized nitrogen involved in triazine rings (C – N=C) and the tertiary nitrogen N-(C)₃ groups, respectively, according to early reference [35]. For pure red P, the high-resolution P 2p orbit in Fig. 3(c) shows two peaks at 130.0 eV and 134.5 eV, which are attributed to elemental P (P⁰) and surface oxides (P–O bonds), respectively based on reference [17]. After sonochemical treatment, the obtained CNP hybrid sheets exhibit the same dominant peak at 130.0 eV as that of red P, confirming the major existence of elemental red P. Moreover, the peak corresponding to surface P–O bonds obviously shifts to lower binding energy at 133.5 eV, which is originated from P–N bonds formed in P-doped g-C₃N₄ [36,37]. This result further confirms that the surface oxides of red P are removed in the CNP composites, and the elemental red P are chemically bonded to the g-C₃N₄ sheets via P–N bonds. As shown in Fig. 3(d), at the interfaces of red P nanoparticles and g-C₃N₄ sheets, the surface P atoms of elemental red P replace the corner or bay carbon in polymeric C–N structures to form P–N bonding [36], resulting in g-C₃N₄ nanosheets *in-situ* surface bonded to elemental red P. The clean surface of red P as well as the obtained intimate heterojunctions between g-C₃N₄ and red P would be beneficial for photocatalytic activity.

The light absorption property of as-prepared samples is also studied by UV-vis DRS spectra, and the results are shown in Fig. 4. Pure g-C₃N₄ shows a typical semiconductor absorption, originating from charge transfer response of g-C₃N₄ from the VB populated by N 2p orbitals to the CB formed by C 2p orbitals [11]. It shows a light absorption edge of about 460 nm, corresponding to the band gap energy of 2.7 eV, which is also consistent with previous studies [38,39]. With the combination of red P, the CNP samples show enhanced VL absorption, and the VL light absorption edge is extended to 700 nm. In addition, the VL absorption intensity is found to increase with the increase of red P amount. Obviously, the extended VL light absorption in the longer wavelength (460–700 nm) is due to the inter-band transition of elemental red P. It is

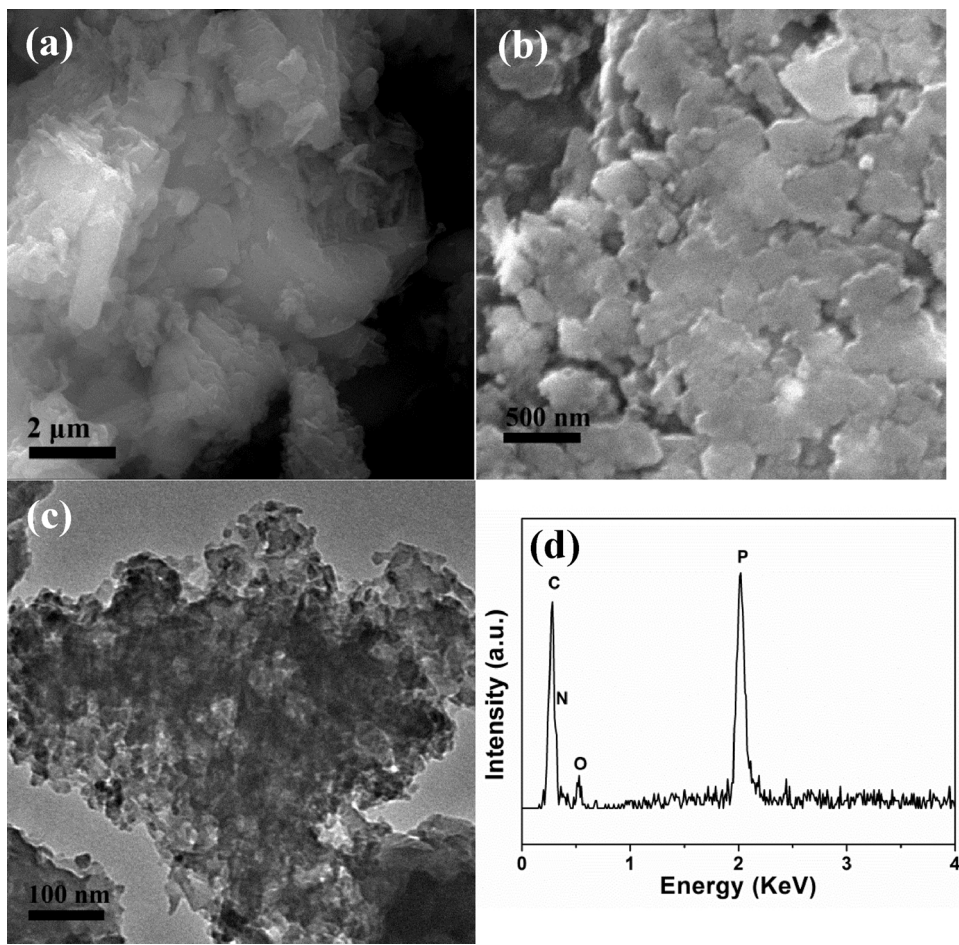


Fig. 2. (a) Typical SEM image of $\text{g-C}_3\text{N}_4$; (b) SEM, (c) TEM and (d) EDX of the as-prepared CNP-0.10.

also noted that the light absorption intensity increases dramatically from CNP-0.5 to CNP-0.1, while only slightly increases from CNP-0.1 to CNP-0.2, probably due to the $\text{g-C}_3\text{N}_4$ sheets are almost covered by red P nanoparticles in the case of CNP-0.15 and CNP-0.2, thus no extra red P is allowed to be loaded onto the $\text{g-C}_3\text{N}_4$ sheets.

To reveal the photoinduced charge separation and transfer efficiency in the CNP composites, the photoelectrochemical study was conducted and the photocurrent response was also recorded. As shown in Fig. 5, the photocurrent responses for the CNP composite electrodes are prompt, steady and reproducible during repeated on/off cycles of the VL light illumination. The $\text{g-C}_3\text{N}_4$ shows moderate photocurrent intensity, while the photocurrent is significantly increased with the combination of red P. The CNP-0.1 exhibits the highest photocurrent density. However, further increase of loaded red P results in the decrease of current density, attributed to the excessive red P in the composites that may completely cover the surface of $\text{g-C}_3\text{N}_4$. Thus, the photocurrent is decreased due to the limited excitation of $\text{g-C}_3\text{N}_4$.

3.2. Photocatalytic H_2 evolution performances

The photocatalytic performances for H_2 production over as-prepared samples under VL irradiation were shown in Fig. 6(a) and (b). Control experiments confirm no H_2 evolution obtained without photocatalysts or light illumination. The pure red P shows weak H_2 evolution activity ($32 \mu\text{mol h}^{-1} \text{g}^{-1}$), while $\text{g-C}_3\text{N}_4$ exhibits obvious H_2 evolution activity ($325.3 \mu\text{mol h}^{-1} \text{g}^{-1}$) under VL irradiation ($\lambda > 420 \text{ nm}$). In the presence of a small amount of red P loading, the photocatalytic activity of the CNP-0.05 sample is remarkably enhanced. Moreover, the photocatalytic activity of the samples further increases with increasing

red P content from CNP-0.05 to CNP-0.1. The highest H_2 -production rate of $1691 \mu\text{mol h}^{-1} \text{g}^{-1}$, obtained for the CNP-0.1 sample, is 5.2 and 52.8 times higher than that of pure $\text{g-C}_3\text{N}_4$ and red P, respectively. The apparent quantum efficiency (AQE) at 420 nm is calculated to be 2.6% by measuring the H_2 production rate under monochromic light ($\lambda = 420 \text{ nm}$) irradiation (Fig. S4). However, in the case of CNP-0.15 and CNP-0.2, further increasing the red P content would lead to the decrease of photocatalytic activity. Therefore, a suitable weight ratio of red P and $\text{g-C}_3\text{N}_4$ is very crucial for optimizing the activity of the CNP composites. In comparison, a physical mixture of red P (0.1 g) and $\text{g-C}_3\text{N}_4$ (0.1 g) only shows a H_2 evolution rate of $298.3 \mu\text{mol h}^{-1} \text{g}^{-1}$, which is even lower than that of pure $\text{g-C}_3\text{N}_4$. This result clearly demonstrates that the $\text{g-C}_3\text{N}_4/\text{red P}$ heterojunctions prepared by sonchemical treatment plays an essential role in the enhancement of photocatalytic H_2 evolution activities.

The stability of CNP-0.1 for H_2 evolution was evaluated by performing recycling experiments under VL irradiation. As shown in Fig. 6(c), the hydrogen evolution yield remains unchanged after three runs, indicating sufficient stability of CNP-0.1 for photocatalytic H_2 evolution. In order to further elucidate the extended photo-response to H_2 evolution in longer wavelength of visible light region, the wavelength dependence of photocatalytic H_2 evolution over CNP-0.1 was investigated in the range of 420–700 nm using various band pass filters ($\lambda = 420, 450, 500, 550, 600, 650$, and 700 nm). As shown in Fig. 6(d), the H_2 production rate is $737.8 \mu\text{mol h}^{-1} \text{g}^{-1}$ under 420 nm irradiation, and this value is gradually decreased to 427.9, 270.8, 236.2, 108.7, 50.2 and $25.1 \mu\text{mol h}^{-1} \text{g}^{-1}$ under wavelength of 450, 500, 550, 600, 650, and 700 nm, respectively. Obviously, the photocatalytic H_2 production rate under different wavelengths is in

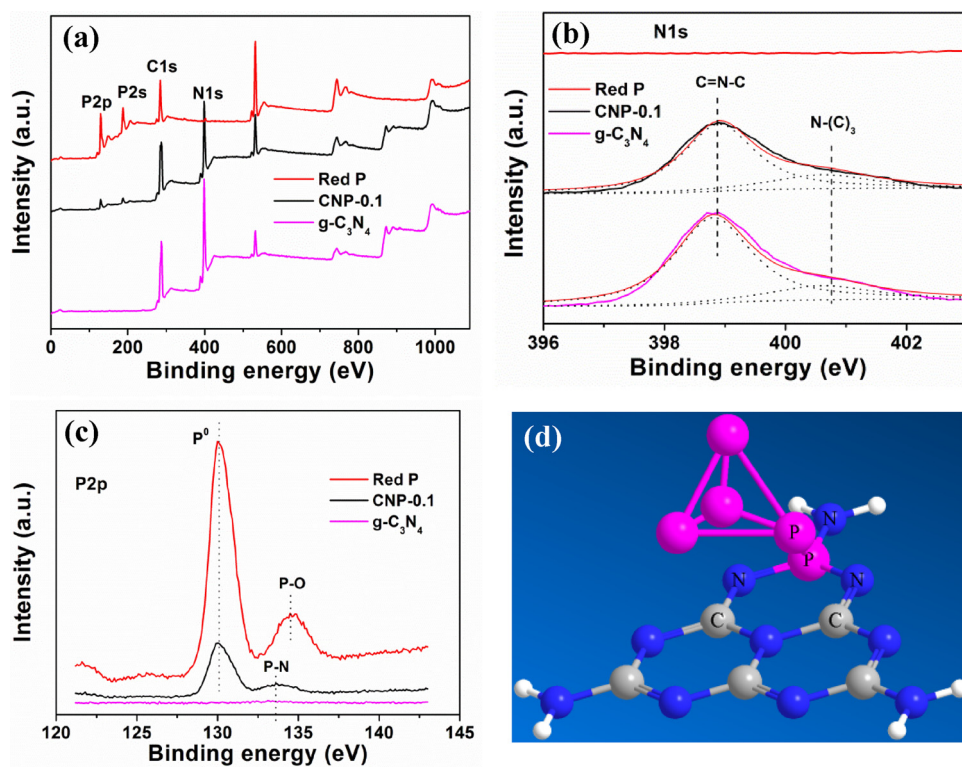


Fig. 3. (a) XPS survey spectra, (b) High-resolution N 1s spectra and (c) High-resolution P 2p spectra of g-C₃N₄, red P and CNP-0.10; (c) Possible bonding states in CNP heterojunctions. (For interpretation of the references to colour in this figure legend, the reader is referred to the web version of this article).

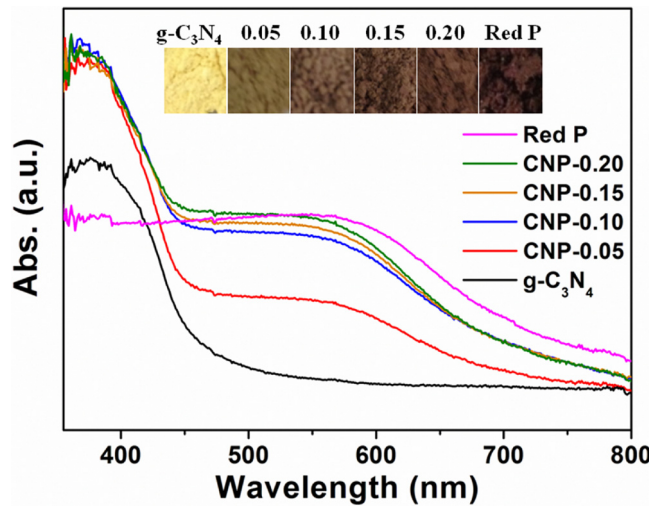


Fig. 4. UV-vis diffuse reflectance spectra of g-C₃N₄, red P and CNP composites. (For interpretation of the references to colour in this figure legend, the reader is referred to the web version of this article).

agreement with its light absorption property, indicating the extended light absorption by CNP is also responsive to photocatalytic H₂ evolution reactions. The longest wavelength used for H₂ evolution is found to be 700 nm with a H₂ production rate of 25.1 $\mu\text{mol h}^{-1} \text{g}^{-1}$. Thus, it is confirmed that CNP hybrid nanosheets exhibits wide-spectral-responsive photocatalytic activity up to 700 nm, which almost covers the whole visible light region, suggesting great potential to be used in solar energy conversion.

3.3. Photocatalytic bacterial inactivation performances

The photocatalytic activity in bacterial inactivation was also

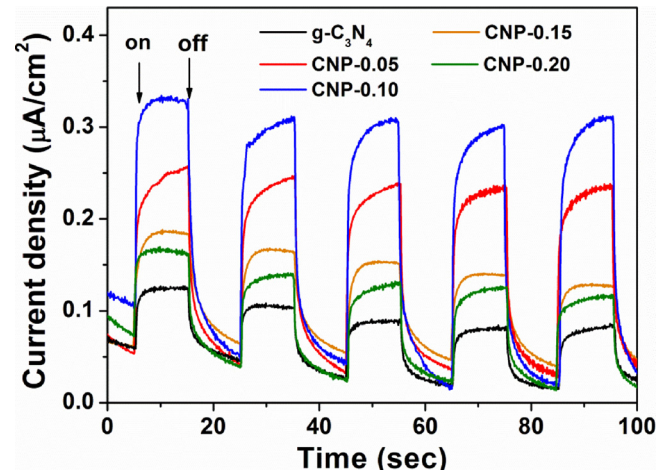


Fig. 5. Transient photocurrent responses of as-prepared CNP composites under VL irradiation ($\lambda > 420 \text{ nm}$).

evaluated by inactivating *E. coli* K-12 as a representative waterborne microorganism. As shown in Fig. 7(a), no bacterial inactivation was found in light control (without photocatalysts) and dark control (without light irradiation) experiments. The pure g-C₃N₄ shows very limited photocatalytic bacterial inactivation activity, and less than 1.5-log cfu/mL *E. coli* K-12 can be inactivated within 120 min of visible light irradiation with comparable results in our previous reference [13]. Interestingly, with the introduction of red P into heterojunctions, the CNP-0.05 exhibits obvious enhanced photocatalytic bacterial inactivation activity of 3.5-log cfu/mL cell reduction within 120 min, and the inactivation efficiency is found to further increase with the increase of red P loading amount. The highest activity is observed for CNP-0.15 sample, with total 7-log cfu/mL cell reduction within 80 min. When further increasing the red P amount, the activity of obtained CNP-0.2

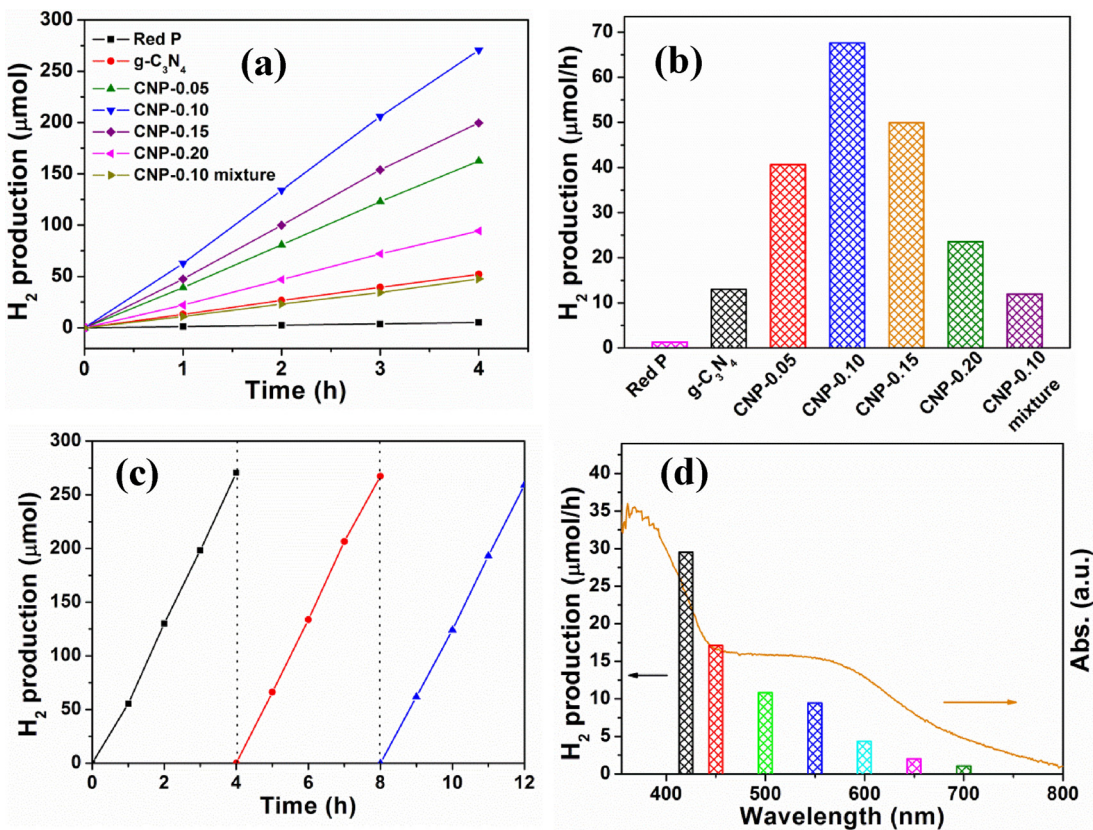


Fig. 6. (a) Photocatalytic H₂ evolution by as-prepared samples under VL irradiation; (b) Normalized H₂ evolution rate within 4 h; (c) Cyclic H₂ evolution curve for CNP-0.10 sample under VL irradiation ($\lambda > 420$ nm); (d) Wavelength-dependent photocatalytic H₂ evolution over CNP-0.10 under different monochromic light irradiation.

sample is decreased, probably due to excess red P would cover the surface of g-C₃N₄ leading to insufficient light absorption and decreased active sites of g-C₃N₄. To quantitatively understand the reaction rate, the inactivation kinetics were modeled with a first-order decay of viability, followed by the presence of a tailing phase in which liberated intracellular components competing with the intact cell for the photocatalytic attack. These results were fitted well ($R^2 = 0.99$) using the model proposed by Geeraerd et al. (Eq. (2)) [40]:

$$N_t = (N_0 - N_{\text{res}}) \times \exp(-k_{\text{max}} \times t) + N_{\text{res}} \quad (2)$$

Where N_t and N_0 was the survival number of cells at reaction time (t) and initial time, respectively; k_{max} denoted the inactivation rate and N_{res} was the residual number of the cells, and the fitted k_{max} values are shown in Fig. S5. The results showed that pure g-C₃N₄ exhibit a k_{max} value of only $0.57 \times 10^{-2} \text{ min}^{-1}$. With the increase of red P amount, the k_{max} values increases from 0.83×10^{-3} to 3.55×10^{-3} , and then decreases to 1.51×10^{-3} for CNP-0.2. Therefore, the CNP-0.15 exhibits significantly enhanced photocatalytic bacterial inactivation efficiency by a factor of 6.23 times higher than that of pure g-C₃N₄. In addition, the CNP-0.15 also exhibits 1.58 times higher activity than that of pure red P ($k = 2.24 \times 10^{-3}$).

To further understand the bacterial inactivation mechanism during the photocatalytic process, scavenging studies was also conducted by using isopropanol, 4-hydroxy-2,2,6,6-tetramethylpiperidinyloxy (TEMPO), Cr(VI), Fe(II)-EDTA and oxalate as ·OH, ·O₂⁻, e⁻, H₂O₂ and h⁺ scavengers, respectively, with the method recommended by our early reference [41]. No bacterial inactivation was observed with the addition of these scavengers (Fig. S6), indicating the present dosage of scavengers would not cause detectable toxicity to the bacterial cells. As shown in Fig. 7(b), with the addition of isopropanol and Cr(VI), the bacterial inactivation efficiency is only slightly decreased, indicating

the ·OH and photo-generated e⁻ play minor role in the bacterial inactivation process. With the addition of Fe(II)-EDTA, TEMPO and oxalate, the inactivation efficiency is decreased significantly, suggesting H₂O₂, ·O₂⁻ and photo-generated h⁺ are important species for the inactivation in this system. It is also noted that the addition of oxalate exhibits the most obvious inhibition effect, suggesting the h⁺ may be the major reactive species and the bacterial cells is inactivated by an oxidative pathway instead of a reduction pathway as the above H₂ evolution process.

To further investigate the bacterial inactivation mechanism, the inactivation experiments was also conducted with different gas bubbling. Fig. 7(c) shows the comparison of photocatalytic bacterial inactivation efficiency under aerobic and anaerobic conditions. It was found that the inactivation efficiency is increased with O₂ bubbling while decreased significantly with N₂ bubbling, indicating O₂ is essential for the oxidative inactivation process in this work, although there are still about 3-log reduction of viable cells under N₂ aeration condition. Further addition of oxalate in the N₂ aeration condition can completely inhibit the disinfection efficiency, which indicates the major reactive species under anaerobic conditions is photo-generated h⁺. To further confirm the oxidative inactivation process, bacterial catalase (CAT) activity was also measured during the inactivation process due to CAT is a well-known antioxidant enzyme to catalyze the decomposition of H₂O₂. A higher level of CAT indicates the bacterial cells are encountering a more significant oxidative stress from the environment. As shown in Fig. 7(d), no CAT activity is induced under dark conditions, while a significant CAT level is found under O₂ aeration condition, confirming the oxidative inactivation of bacterial cells rather than the reductive inactivation. More interesting, an obvious CAT level is also induced under N₂ aeration condition without O₂. These results indicate that the photo-generated h⁺ but not e⁻ plays the major role in bacterial

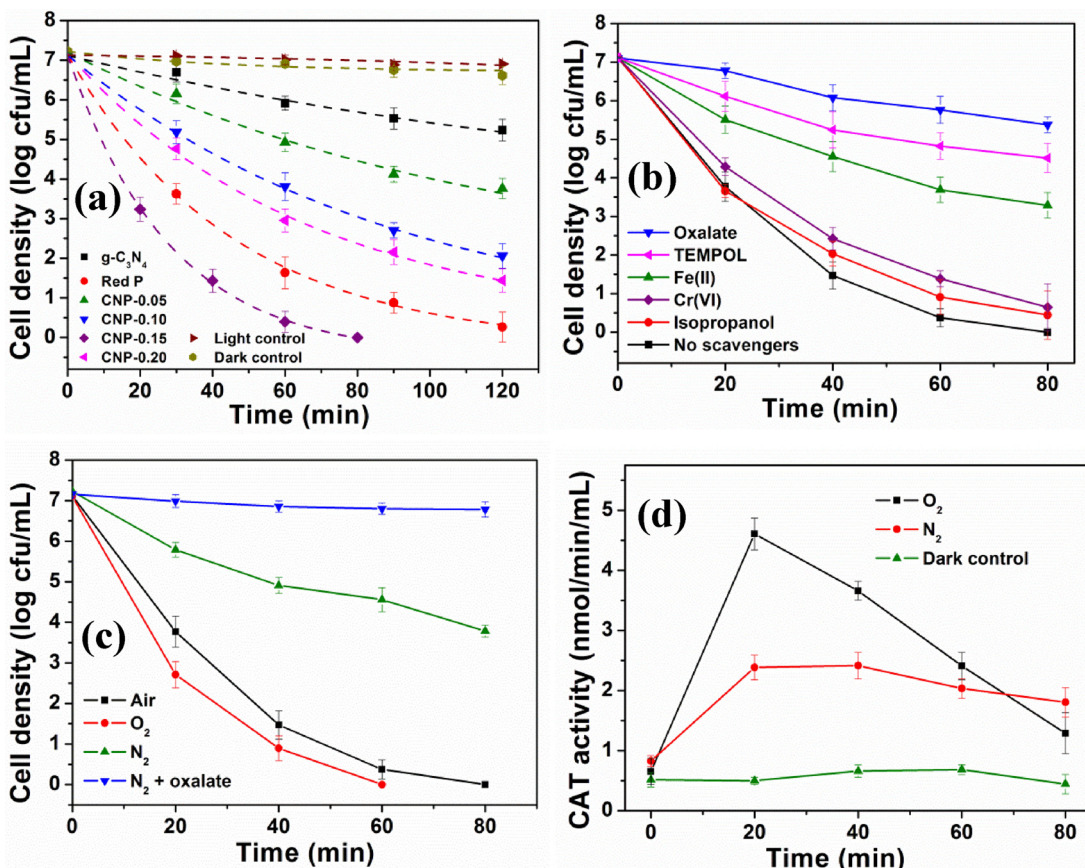


Fig. 7. (a) Photocatalytic inactivation efficiencies against *E. coli* K-12 by as-prepared samples with kinetic modeling; (b) Photocatalytic inactivation efficiencies with different scavengers (0.05 mM Cr(VI), 0.5 mM isopropanol, 0.5 mM sodium oxalate, 0.5 mM TEMPOL, 0.1 mmol/L Fe(II)-EDTA); (c) Photocatalytic inactivation efficiencies under different gas bubbling; (d) Induction of CAT activity under photocatalytic inactivation of *E. coli* K-12 by CNP-0.15 in aerobic and anaerobic conditions.

inactivation in this system, which is different from the H₂ evolution applications. The h⁺ and its derived H₂O₂ could directly inactivate the cells and cause the induction of CAT levels.

The wavelength-dependent photocatalytic bacterial inactivation was also investigated by using CNP-0.15 as the photocatalyst. As shown in Fig. 8(a), with monochromatic light irradiation ($\lambda = 420$ nm), the bacterial cells could also be inactivated, but the efficiency is much lower than that of visible light irradiation ($\lambda > 420$ nm). In addition, with longer wavelength light irradiation, the inactivation efficiency decreased significantly, due to the lower excited photon energy causing

the high rate of charge carriers recombination. It is also noted that even the light wavelength is extended to 700 nm, the bacterial cells still can be inactivated, and the inactivation efficiency under different wavelengths matches well with its light absorption property. These results indicate that the as-prepared CNP composites indeed possess wide-spectral-responsive photocatalytic activity not only for H₂ evolution but also for bacterial inactivation. To further evaluate the photocatalytic stability, the bacterial inactivation procedure was also repeated five times with the same CNP-0.15 sample (Fig. 8(b)). Results showed that no obvious decrease of inactivation efficiency was observed in the first

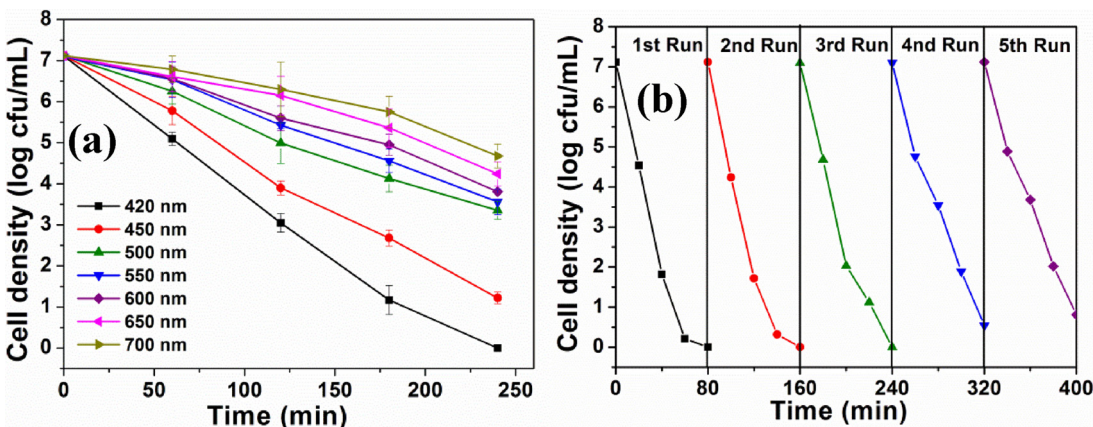


Fig. 8. (a) Wavelength-dependent photocatalytic inactivation against *E. coli* K-12 by CNP-0.15 under different monochromic light irradiation; (b) Recycling experiments of photocatalytic inactivation against *E. coli* K-12 by CNP-0.15 under VL irradiation ($\lambda > 420$ nm).

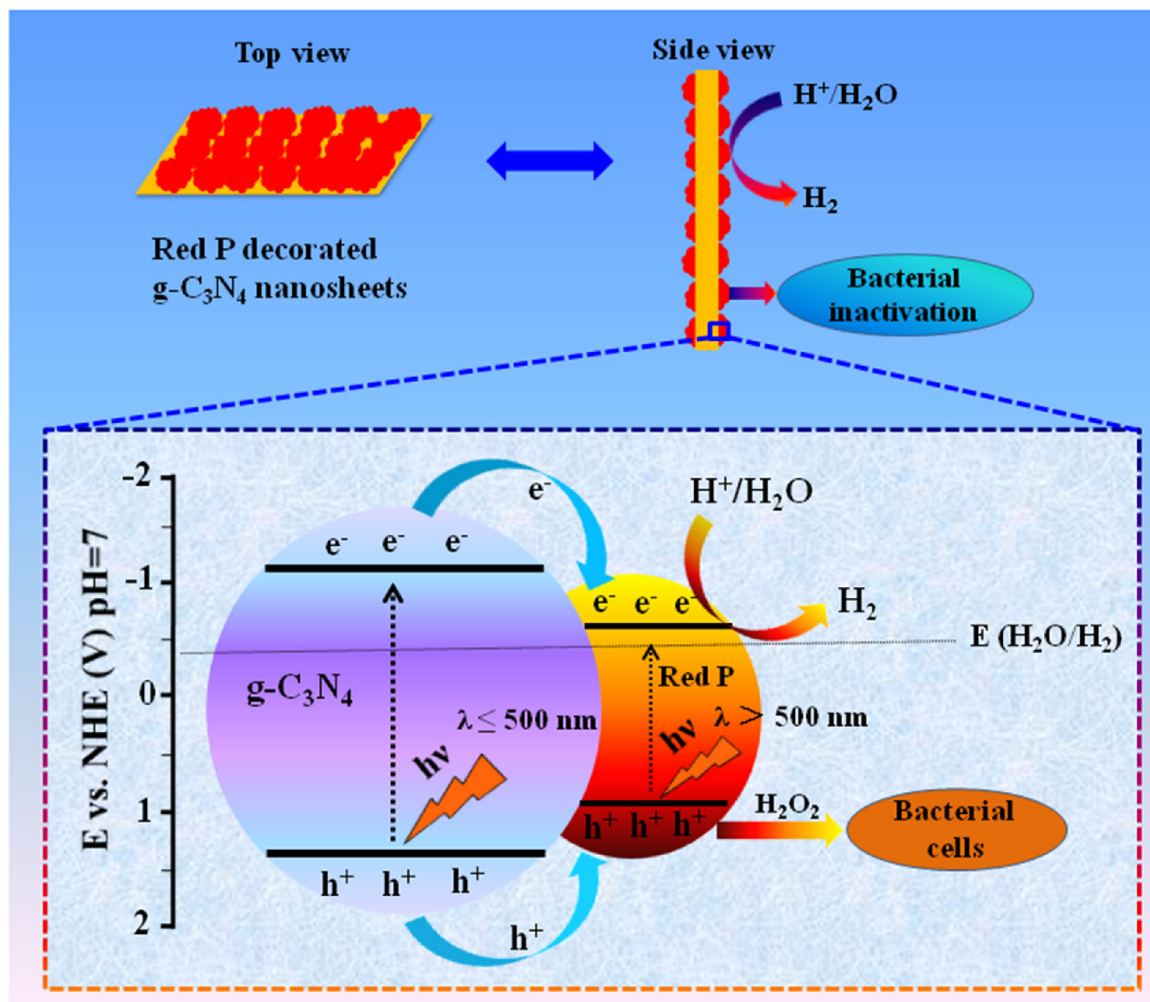


Fig. 9. Schematic illustration of the formation of type I heterojunction and proposed charge separation mechanism in the CNP heterostructures under VL irradiation.

three runs, confirming the high photo-stability of CNP. However, the inactivation efficiency became slightly decrease in the fourth and fifth runs, which may be due to the loss of catalysts during the repeated cycling experiments.

3.4. Possible photocatalytic mechanisms of type I band alignment

To understand the effects of the CNP heterojunctions on the separation of photo-generated e⁻-h⁺ pairs, the band structures of g-C₃N₄ and red P were studied respectively. It has been reported that the conduction band (CB) of red P locates was at about -0.62 V vs. NHE [19], and the valence band (VB) locates at about 1.08 V vs. NHE. In addition, the CB and VB potentials of g-C₃N₄ are reported to be -1.13 V and 1.57 V vs. NHE, respectively [42]. Obviously, the CB potential level of g-C₃N₄ is more negative than that of red P so that photo-generated e⁻ could migrate from g-C₃N₄ to red P driven by the contact electric field. While the VB potential level of g-C₃N₄ is more positive than that of red P so that photo-generated h⁺ could also migrate from g-C₃N₄ to red P, forming a straddled band alignment (i.e. type I band alignment), as shown in Fig. 9. When the irradiation wavelength is less than 500 nm, both the g-C₃N₄ and the red P can be excited. The photo-generated e⁻ is transferred from the CB of g-C₃N₄ to red P, while the photo-generated h⁺ is also transferred from the VB of g-C₃N₄ to red P. Although both the photo-generated charge carries transfer from g-C₃N₄ to red P through the interface, the difference between the migration rates of electrons and holes leads to efficient separation of the charge carriers at the interface. Moreover, the unique configuration of the red P layer covered

g-C₃N₄ nanosheets allows both the charge carriers to expose to the liquid phase and effectively involve in the later photocatalytic reactions, resulting in the improvement of photocatalytic activity. As shown in Fig. 9, the type-I red P/g-C₃N₄ heterojunction allows most of the surface-trap states of the g-C₃N₄ to be passivated by red P shell. Thus, the confined electrons and holes in the g-C₃N₄ core might tunnel through the red P shell to the outer surface for photocatalytic H₂ evolution and bacterial inactivation, respectively. In addition, the pristine photocatalytic activity of red P further promotes charge carries generation, cooperatively enhance the H₂ evolution and bacterial inactivation activity. When the irradiation wavelength is higher than 500 nm ($\lambda > 500$ nm), the photocatalytic activity is mainly attributed to the function of red P to absorb the photons with long wavelength. In addition, it has been reported that P-doped g-C₃N₄ could extend the light absorbance in the visible region up to 800 nm [36,37]. Therefore, the surface P doping in the g-C₃N₄ also contributes the photocatalytic activity by electron transfer from surface P doped g-C₃N₄ to elemental red P in the CNP composites. It should be noted that the optimized ratio between g-C₃N₄ and red P for H₂ production and bacterial inactivation is different. The highest photocatalytic activity for H₂ production is obtained by sample CNP-0.1, while it is CNP-0.15 with higher red P amounts for bacterial inactivation. This is because the pristine red P has significantly higher photocatalytic bacterial inactivation activity but much lower photocatalytic H₂ production activity than that of g-C₃N₄. Therefore, compared with H₂ production, the optimized ratio for bacterial inactivation is obtained by sample with higher red P amounts (i.e. CNP-0.15). The type I heterojunction and intrinsic high activity of

pristine red P collectively contributes the high activity for bacterial inactivation.

To reveal the migration, transfer and recombination processes of photogenerated e^- - h^+ pairs in the CNP composites, photoluminescence (PL) technique was employed according to the reference [43]. The PL spectra of pure g-C₃N₄, CNP-0.1 and CNP-mixture were presented in Fig. S7. According to the previous reference [44], the excitation wavelength of g-C₃N₄ is 375 nm. It is found that pure g-C₃N₄ shows a strong, wide peak in the PL spectrum, while the PL peak of the CNP-0.1 composites decrease remarkably compared with the pure g-C₃N₄, indicating the recombination of electrons and holes is hindered significantly. In contrast, the PL intensity of the CNP-mixture remains almost the same as that of pure g-C₃N₄, suggesting the photogenerated e^- - h^+ pairs in this case are mostly recombined as that in pure g-C₃N₄. This result confirms that the type I heterojunction in the CNP composites synthesized by sonochemical method facilitates the migration of charge carriers.

In order to further prove that the type I heterojunction was existed in the CNP heterostructure to hinder the recombination of the photo-excited e^- - h^+ pairs, the interface charge separation efficiency is further investigated by the typical electrochemical impedance spectra (presented as Nyquist plots), and the plots of g-C₃N₄ and CNP-0.1 electrodes before and after VL irradiation were shown in Fig. S8. The arc radius on the EIS Nyquist plot can reflect the reaction rate to the surface of the electrode. The smaller arc radius indicates a more effective separation of photogenerated e^- - h^+ pairs and a higher efficiency of charge immigration across the electrode/electrolyte interface according to the references [45,46]. The arc radii of CNP-0.1 electrode are smaller than that of pure g-C₃N₄ electrode, suggesting that the CNP heterostructures can make the separation and immigration of photogenerated e^- - h^+ pairs more efficient, which is in good accordance with the result of photocurrent measurement and PL investigation. Therefore, it can be concluded that the formation of the CNP sheets-like type I heterojunction between g-C₃N₄ and red P greatly facilitates separation and depresses the recombination of photogenerated e^- - h^+ pairs, thus significantly enhancing the photocatalytic activity, while the efficient utilization of photogenerated e- from both the g-C₃N₄ and the narrow band gap of red P results in the considerable photocatalytic activity in longer wavelength region. Most importantly, it is noted that most of the previous study has emphasized the utilization of type II heterojunction (i.e. staggered gap) for constructing composite photocatalyst [47,48]. However, the present study indicates that the type I heterojunction (i.e. straddling gap) may be more important in some cases with special core/shell configuration, since both electrons and holes could be rationally driven to the shell by the built-in energy potential, which promotes the separation of the photoexcited charge carriers and efficiently facilitates charge transfer to the shell layer to enhance the redox reaction. When the shell layer is a narrow band gap semiconductor, such as the red P, a high-efficient wide-spectral-responsive photocatalyst can be achieved by applying the type I heterojunction to construct composite photocatalysts.

4. Conclusions

In summary, g-C₃N₄/red P hybrid nanosheets have been fabricated in one step at room temperature, using sonochemical treatment as a “green” and environmental benign synthetic method. The exfoliation of layered g-C₃N₄ and size reduction of red P particles are achieved simultaneously, resulting in red P nanoparticles anchored onto the g-C₃N₄ nanosheets to form intimate heterojunctions via P–N chemical bonding. The as-prepared CNP heterojunctions exhibit significantly enhanced photocatalytic activity for H₂ evolution under VL irradiation, which is about 5.2 and 52.8 times higher than that of pure g-C₃N₄ and red P, respectively. In addition, the CNP also shows much high enhanced photocatalytic activity to bacterial inactivation, with about 6.23 and 1.58 times higher than that of pure g-C₃N₄ and red P, respectively.

Most importantly, the CNP shows wide-spectral-responsive photocatalytic activity up to 700 nm for both H₂ evolution and bacterial inactivation. The enhancement is mainly attributed to the type I junctions formed between g-C₃N₄ and red P, which facilitates the interface charge separation and extends the light response by efficiently utilizing the photogenerated e^- excited from both g-C₃N₄ and red P. This work will provide useful information not only for the synthesis of metal-free heterojunctions by employing the facile and “green” sonochemical methods, but also for the development of wide-spectral-responsive photocatalysts using type I band alignment combined with the narrow band gap feature of elemental red P.

Acknowledgements

This work was supported by the National Natural Science Foundation of China (No. 41425015, 21607028 and 41573086) and the Research Grant Council of Hong Kong SAR Government (No. T23-407/13-N) to T.C. An, W.J. Wang, G.Y. Li and J.C. Yu, respectively. P.K. Wong was supported by CAS/SAFEA International Partnership Program for Creative Research Teams (2015HSC-UE004) of Chinese Academy of Sciences.

Appendix A. Supplementary data

Supplementary material related to this article can be found, in the online version, at doi:<https://doi.org/10.1016/j.apcatb.2018.07.004>.

References

- [1] X.B. Chen, S.H. Shen, L.J. Guo, S.S. Mao, Chem. Rev. 110 (2010) 6503–6570.
- [2] S.J.A. Moniz, S.A. Shevlin, D.J. Martin, Z.X. Guo, J.W. Tang, Energy Environ. Sci. 8 (2015) 731–759.
- [3] X. Li, J.G. Yu, J.X. Low, Y.P. Fang, J. Xiao, X.B. Chen, J. Mater. Chem. A 3 (2015) 2485–2534.
- [4] W.J. Wang, G.Y. Li, D.H. Xia, T.C. An, H.J. Zhao, P.K. Wong, Environ. Sci.: Nano 4 (2017) 782–799.
- [5] O.K. Dalrymple, E. Stefanakos, M.A. Trotz, D.Y. Goswami, Appl. Catal. B: Environ. 98 (2010) 27–38.
- [6] P. Ganguly, C. Byrne, A. Breen, S.C. Pillai, Appl. Catal. B: Environ. 225 (2018) 51–75.
- [7] T.C. An, H.J. Zhao, P.K. Wong, Advances in Photocatalysis Disinfection, Springer, Berlin, Heidelberg, 2016.
- [8] J.S. Jang, S.H. Choi, H.G. Kim, J.S. Lee, J. Phys. Chem. C 112 (2008) 17200–17205.
- [9] J. Ng, S.P. Xu, X.W. Zhang, H.Y. Yang, D.D. Sun, Adv. Funct. Mater. 20 (2010) 4287–4294.
- [10] K.E. deKrafft, C. Wang, W.B. Lin, Adv. Mater. 24 (2012) 2014–2018.
- [11] X.C. Wang, K. Maeda, A. Thomas, K. Takanabe, G. Xin, J.M. Carlsson, K. Domen, M. Antonietti, Nat. Mater. 8 (2009) 76–80.
- [12] Y. Wang, X.C. Wang, M. Antonietti, Angew. Chem. Int. Ed. 51 (2012) 68–89.
- [13] G.Y. Li, X. Nie, J.Y. Chen, Q. Jiang, T.C. An, P.K. Wong, H.M. Zhang, H.J. Zhao, H. Yamashita, Water Res. 86 (2015) 17–24.
- [14] G.Y. Li, X. Nie, Y.P. Gao, T.C. An, Appl. Catal. B: Environ. 180 (2016) 726–732.
- [15] W.J. Wang, T.C. An, G.Y. Li, D.H. Xia, H.J. Zhao, J.C. Yu, P.K. Wong, Appl. Catal. B: Environ. 217 (2017) 570–580.
- [16] F. Wang, W.K.H. Ng, J.C. Yu, H.J. Zhu, C.H. Li, L. Zhang, Z.F. Liu, Q. Li, Appl. Catal. B: Environ. 111–112 (2012) 409–414.
- [17] F. Wang, C.H. Li, Y.C. Li, J.C. Yu, Appl. Catal. B: Environ. 119–120 (2012) 267–272.
- [18] Z.R. Shen, S.T. Sun, W.J. Wang, J.W. Liu, Z.F. Liu, J.C. Yu, J. Mater. Chem. A 3 (2015) 3285–3288.
- [19] D.H. Xia, Z.R. Shen, G.C. Huang, W.J. Wang, J.C. Yu, P.K. Wong, Environ. Sci. Technol. 49 (2015) 6264–6273.
- [20] Y.P. Yuan, S.W. Cao, Y.S. Liao, L.S. Yin, C. Xue, Appl. Catal. B: Environ. 140–141 (2013) 164–168.
- [21] L. Jing, R.X. Zhu, D.L. Phillips, J.C. Yu, Adv. Funct. Mater. 27 (2017) 1703484.
- [22] P. Niu, L. Zhang, G. Liu, H.M. Cheng, Adv. Funct. Mater. 22 (2012) 4763–4770.
- [23] X. Zhang, X. Xie, H. Wang, J. Zhang, B. Pan, Y. Xie, J. Am. Chem. Soc. 135 (2012) 18–21.
- [24] Q.Y. Lin, L. Li, S.J. Liang, M.H. Liu, J.H. Bi, L. Wu, Appl. Catal. B: Environ. 163 (2015) 135–142.
- [25] X. She, H. Xu, Y. Xu, J. Yan, J. Xia, L. Xu, Y. Song, Y. Jiang, Q. Zhang, H. Li, J. Mater. Chem. A 2 (2014) 2563–2570.
- [26] Q.L. Ma, R. Xiong, B.G. Zhai, Y.M. Huang, Appl. Surf. Sci. 324 (2015) 842–848.
- [27] Y.Y. Huang, E.M. Terentjev, Polymers 4 (2012) 275–295.
- [28] X. Wang, S. Blechert, M. Antonietti, ACS Catal. 2 (2012) 1596–1606.
- [29] W.J. Wang, J.C. Yu, Z.R. Shen, D.K.L. Chan, T. Gu, Chem. Commun. 50 (2014) 10148–10150.
- [30] W.J. Wang, Y. Yu, T.C. An, G.Y. Li, H.Y. Yip, J.C. Yu, P.K. Wong, Environ. Sci.

- Technol. 46 (2012) 4599–4606.
- [31] Z.A. Lan, G.G. Zhang, X.C. Wang, Appl. Catal. B: Environ. 192 (2016) 116–125.
- [32] X. Wang, X. Chen, A. Thomas, X. Fu, M. Antonietti, Adv. Mater. 21 (2009) 1609–1612.
- [33] Y.J. Zhou, L.G. Zhang, J.J. Liu, X.Q. Fan, B.Z. Wang, M. Wang, W.C. Ren, J. Wang, M.L. Li, J.L. Shi, J. Mater. Chem. A 3 (2015) 3862–3867.
- [34] M.R. Ahsan, M.A. Uddin, M.G. Mortuza, Indian J. Pure Appl. Phys. 43 (2005) 89–99.
- [35] Q.Y. Lin, L. Li, S.J. Liang, M.H. Liu, J.H. Bi, L. Wu, Appl. Catal. B: Environ. 163 (2015) 135–142.
- [36] Y.J. Zhang, T. Mori, J.H. Ye, M. Antonietti, J. Am. Chem. Soc. 132 (2010) 6294–6295.
- [37] L.G. Zhang, X.F. Chen, J. Guan, Y.J. Jiang, T.G. Hou, X.D. Mu, Mater. Res. Bull. 48 (2013) 3485–3491.
- [38] S.Z. Hu, L. Ma, J.Q. You, F.Y. Li, Z.P. Fan, F. Wang, D. Liu, J.Z. Gui, RSC Adv. 4 (2014) 21657–21663.
- [39] H. Zhao, Y.M. Dong, P.P. Jiang, H.Y. Miao, G.L. Wang, J.J. Zhang, J. Mater. Chem. A 3 (2015) 7375–7381.
- [40] A.H. Geeraerd, C.H. Herremans, J.F. Van Impe, Int. J. Food Microbiol. 59 (2000) 185–209.
- [41] W.J. Wang, L.Z. Zhang, T.C. An, G.Y. Li, H.Y. Yip, P.K. Wong, Appl. Catal. B: Environ. 108–109 (2011) 108–116.
- [42] L. Ge, C. Han, J. Liu, Appl. Catal. B: Environ. 108–109 (2011) 100–107.
- [43] Y.X. Guo, H.W. Huang, Y. He, N. Tian, T.R. Zhang, P.K. Chu, Q. An, Y.H. Zhang, Nanoscale 7 (2015) 11702–11711.
- [44] D.M. Chen, K.W. Wang, W.Z. Hong, R.L. Zong, W.Q. Yao, Y.F. Zhu, Appl. Catal. B: Environ. 166–167 (2015) 366–373.
- [45] W.J. Wang, Y.C. Li, Z.W. Kang, F. Wang, J.C. Yu, Appl. Catal. B: Environ. 182 (2016) 184–192.
- [46] S.J. Hong, S. Lee, J.S. Jang, J.S. Lee, Energy Environ. Sci. 4 (2011) 1781–1787.
- [47] J.S. Zhang, M.W. Zhang, R.Q. Sun, X.C. Wang, Angew. Chem. Int. Ed. 51 (2012) 10145–10149.
- [48] A. Kar, S. Sain, D. Rossouw, B.R. Knappett, S.K. Pradhan, G.A. Botton, A.E.H. Wheatley, J. Alloy. Compound. 698 (2017) 944–956.